

# Pressure Induced Unstable Electronic States upon Correlated Nickelates Metastable Perovskites as Batch Synthesized via Heterogeneous Nucleation

HPSTAR  
961-2020

Jikun Chen,\* Ziang Li, Hongliang Dong,\* Jianing Xu, Vei Wang,\* Zhenjie Feng, Zhiqiang Chen, Bin Chen, Nuofu Chen, and Ho-Kwang Mao

Establishing condensed matters at their thermodynamically metastable or unstable structures demonstrates merit in the adjustability of their electronic structures, benefiting the discovery of emerging new material functionalities and applications. Herein, a molten-salt assisted heterogeneous nucleation approach is demonstrated to significantly improve the effectiveness in batch synthesis of metastable perovskites correlated oxides, such as rare-earth nickelates ( $ReNiO_3$ ) with various rare-earth compositions. In contrast to their conventional synthesis via solid state reactions, herein the metastable  $ReNiO_3$  is heterogeneously precipitated together with potassium chloride (KCl) within the liquid phase of KCl molten-salt that effectively dissolves the Ni-/Re- precursors and largely enhances their reaction homogeneity. With this solid base overcoming their synthesis metastabilities, the beyond conventional electronic transportation of  $ReNiO_3$  under high pressure is explored. It breaks the conventional thermodynamic equilibrium and triggers the formation of new electronic structures associated with unstable insulating and metallic  $SmNiO_3$  beyond already known manners. The unstable insulating  $SmNiO_3$  exhibits nontemperature-dependent transportation character similar to saturation or bad metals but preserves 2–3 orders higher electronic conductivity, while a kinetic related hysteresis is observed in the temperature-dependent transportations of the unstable metallic  $SmNiO_3$ . These discoveries with nonequilibrium correlated materials are worthy to be explored further.

minimum energy principle that restricts the achievable crystal structures at a given material composition.<sup>[1–3]</sup> It effectively broadens the adjustability in the electronic structures and transportation properties for semiconductors,<sup>[4–6]</sup> shedding a light on the discovery of emerging new materials functionalities that does not exist in conventional equilibrium condensed matters. As one of the most representative metastable quantum materials, the perovskite structured rare-earth nickelates ( $ReNiO_3$ ) exhibit complicated multiple electronic states that are ultrasensitive to external stimulus, such as temperature,<sup>[7–11]</sup> electronic polarization,<sup>[12]</sup> chemical<sup>[13–16]</sup> or electrochemical doping,<sup>[17–19]</sup> structural distortions,<sup>[20–26]</sup> etc. Triggering the electronic transitions among the multiple quantum states of  $ReNiO_3$  or hydrogenated  $ReNiO_3$  enriches new applications in electron correlated electronics, such as correlated logical devices,<sup>[12]</sup> neuron-synapse quantum computing,<sup>[16]</sup> correlated proton conductors,<sup>[15]</sup> weak current ocean sensor,<sup>[17]</sup> and biosensors.<sup>[18]</sup>

It is worth noting that the complexity in the electro-/magnetoquantum states within  $ReNiO_3$  originates from their

electronic orbital configurations as largely determined by the structural distortions of  $NiO_6$  octahedron at high tolerance to metastability.<sup>[7,10]</sup> For example, the electronic energy gap splits within the hybridized O-2p and Ni-3d orbitals can be effectively

## 1. Introduction

Establishing condensed matters at their thermodynamically metastable or unstable status can break the conventional

Prof. J. Chen, Z. Li  
School of Materials Science and Engineering  
University of Science and Technology Beijing  
Beijing 100083, China  
E-mail: jikunchen@ustb.edu.cn

Dr. H. Dong, J. Xu, Z. Feng, Dr. Z. Chen, Dr. B. Chen, Dr. H.-K. Mao  
Center for High Pressure Science and Technology Advanced Research  
Shanghai 201203, China  
E-mail: hongliang.dong@hpstar.ac.cn

 The ORCID identification number(s) for the author(s) of this article can be found under <https://doi.org/10.1002/adfm.202000987>.

DOI: 10.1002/adfm.202000987

Prof. V. Wang  
Department of Applied Physics  
Xi'an University of Technology  
Xi'an 710054, China  
E-mail: wangvei@icloud.com, wangvei@xaut.edu.cn

Dr. Z. Feng  
Materials Genome Institute  
Shanghai University  
Shanghai 200444, China

Prof. N. Chen  
School of Renewable Energy  
North China Electric Power University  
Beijing 102206, China

widened via bending more the Ni–O–Ni bonds, resulting in widely adjustable metal to insulator transitions (MIT)<sup>[7]</sup> and thermistor transportation behaviors.<sup>[10,11]</sup> Nevertheless, the intrinsic high metastability within *ReNiO*<sub>3</sub> meanwhile enlarges the difficulties in their material synthesis, which is by far one of the most critical bottlenecks that impede their practical applications in correlated electronics.<sup>[7–11,27]</sup> It is not possible to synthesize *ReNiO*<sub>3</sub> (except for *LaNiO*<sub>3</sub>) via conventional solid-state chemical reactions, owing to the positive magnitude in their formation free energy ( $\Delta G$ ).<sup>[7,27]</sup> Although *ReNiO*<sub>3</sub> with stable MIT behaviors were previously synthesized via high oxygen-pressure solid state reactions,<sup>[7–9,22–26]</sup> their batch synthesis catering device applications is yet rather difficult. The main difficulties are associated with the low homogeneity and ineffective diffusion among the reactant precursors during solid state reactions, while mechanical agitation is nearly impossible at high oxygen pressures and high temperatures.

In this work, we largely improve the effectiveness in batch synthesis of *ReNiO*<sub>3</sub> with adjustable rare-earth compositions, by developing a molten-salt assisted heterogeneous nucleation (MSAHN) synthetic approach. In contrast to the previous high pressure solid state reactions, herein the *Re* and *Ni* containing precursors are homogeneously dissolved within the liquid phase molten-salt composed of potassium chloride (KCl). Utilizing the surface coherency and chemical bonding between *ReNiO*<sub>3</sub> (010) and KCl (001), the powder of metastable *ReNiO*<sub>3</sub> is further heterogeneously coprecipitated together with KCl by descending temperature below the melting point of the molten salt, and separated out simply via water rinsing. Beyond the conventional explorations of *ReNiO*<sub>3</sub> in their metastable states, we further trigger their unstable electronic orbital configurations by externally imparting high pressures up to 20 GPa, and in situ investigate their resultant electronic transportations. Combining the elevated thermodynamic instability via pressure regulations with their intrinsic orbital correlations and transitions, we discover distinguished transportation characters within the unstable insulating and metallic phases *ReNiO*<sub>3</sub> beyond ones already known previously.

## 2. Results and Discussion

The central issue in synthesizing metastable *ReNiO*<sub>3</sub> (*Re* ≠ *La*) is to reduce their positive formation free energies ( $\Delta G$ ) to negative magnitudes and thermodynamically draw the potential towards the formation of their distorted perovskite phase.<sup>[7,11,27]</sup> We notice that the  $\Delta G$  in crystal growth can be more reduced via well designed heterogeneous nucleation processes,<sup>[11,20]</sup> e.g., by introducing a postremovable heterogeneous seed crystal to facilitate the nucleation of metastable *ReNiO*<sub>3</sub>. The crystalline KCl is expected to be such a candidate, owing to the following two reasons. 1) As illustrated in **Figure 1a–c**, rotating the KCl (001) anticlockwise by 35.9° results in perfect lattice match with the plane of *SmNiO*<sub>3</sub> (010), resulting in a reduction in  $\Delta G$  by 0.28 J m<sup>−2</sup> at their coherent growth estimated by first principle calculations (as more details shown in Section S1, Supporting Information). Noticing their typical magnitude in synthetic metastability of ≈10<sup>1</sup> kJ per mole,<sup>[27]</sup> a spontaneous nucleation of *ReNiO*<sub>3</sub> on KCl seed crystals with 10<sup>1</sup>–10<sup>2</sup> nm in scale is

possible. 2) It is possible to in situ precipitate the KCl as seed crystal from its melt by descending temperature across 773 °C together with the metastable *ReNiO*<sub>3</sub>, while the solidified KCl can be easily dissoluble in water to filter out *ReNiO*<sub>3</sub>.

Following the above consideration, we developed a KCl molten-salt assisted heterogeneous nucleation strategy to synthesize the powder of metastable *ReNiO*<sub>3</sub> via the three steps as illustrated in **Figure 1d**. In the first step, the oxide precursors, such as *Re*<sub>2</sub>*O*<sub>3</sub> and NiO, are mixed at the stoichiometry ratio together with the KCl inside a quartz crucible. The crucible was heated to temperatures beyond 800 °C at 10 MPa oxygen pressure to completely melt the KCl and dissolve the oxide precursors. In the second step, the melt was slowly cooled down below the melting point of the molten salt, in which process the metastable *ReNiO*<sub>3</sub> coprecipitate heterogeneously together with the KCl seed crystal. In the third step, the final solidified material cooling to room temperature is rinsed in water under ultrasonic for several times to dissolve KCl and separate out the powder of *ReNiO*<sub>3</sub>.

As-proposed synthetic approach was first applied to *SmNiO*<sub>3</sub>. In **Figure 2a**, we compare the X-ray diffraction (XRD) patterns of the oxide final product obtained under different representative reaction conditions (see their indexation **Figure S5**, Supporting Information). It is worth noting that the desired perovskite phase *SmNiO*<sub>3</sub> is only obtained at the presence of the KCl molten-salt and applying high oxygen pressure during the molten salt reactions, while the absence of their each results in mixtures of *Re*<sub>2</sub>*O*<sub>3</sub> and NiO as final products. The successfully synthesized powder of metastable perovskite *SmNiO*<sub>3</sub> exhibits cubic shape with an edge length of 1–2 μm, as its morphology demonstrated by the scanning electron microscopy (SEM) observations in **Figure 2b**. Its cation stoichiometry was further confirmed by performing energy dispersion spectrum (EDS) as shown in **Figure S3** (Supporting Information). Compared to the previously synthesis of *ReNiO*<sub>3</sub> via solid-state reactions, the *Ni*- and *Re*-containing precursors can more homogeneously react via dissolving within the liquid phase of the KCl molten salt. This could largely enhance the tolerance in the powder sizes and dispersions of the used precursors compared to the previously used solid state reactions, as the presently used precursor exhibit much larger powder size (see **Figure S4**, Supporting Information) than the *SmNiO*<sub>3</sub> final product. After the synthesis, as-used KCl molten salt was completely removed from the final product via several cycles of ultrasonic water rinsing.

To characterize the metal to insulator transition properties, as-synthesized *SmNiO*<sub>3</sub> powder was compressed and sintered into polycrystalline bulk samples. **Figure 3a** shows the typical temperature dependence of resistivity (*R*–*T*) for the *SmNiO*<sub>3</sub> polycrystalline bulk sample, while its cross-sectional SEM morphology is shown by the inset. An abrupt transition in the electronic transportation from insulator (or semiconductor) to metal is observed for the presently grown *SmNiO*<sub>3</sub> bulk sample when elevating temperature across a *T*<sub>MIT</sub> of 100 °C, which is in agreement with the previous reports for polycrystalline *SmNiO*<sub>3</sub>.<sup>[7–9,12]</sup> We further extend the MSAHN approach in the synthesis of other *ReNiO*<sub>3</sub> with single or binary rare-earth compositions, such as *EuNiO*<sub>3</sub>, *GdNiO*<sub>3</sub>, *Nd*<sub>*x*</sub>*Sm*<sub>1–*x*</sub>*NiO*<sub>3</sub> and *Eu*<sub>*x*</sub>*Sm*<sub>1–*x*</sub>*NiO*<sub>3</sub>, (see their XRD patterns in **Figure S5**, Supporting Information). The high flexibility in regulating the

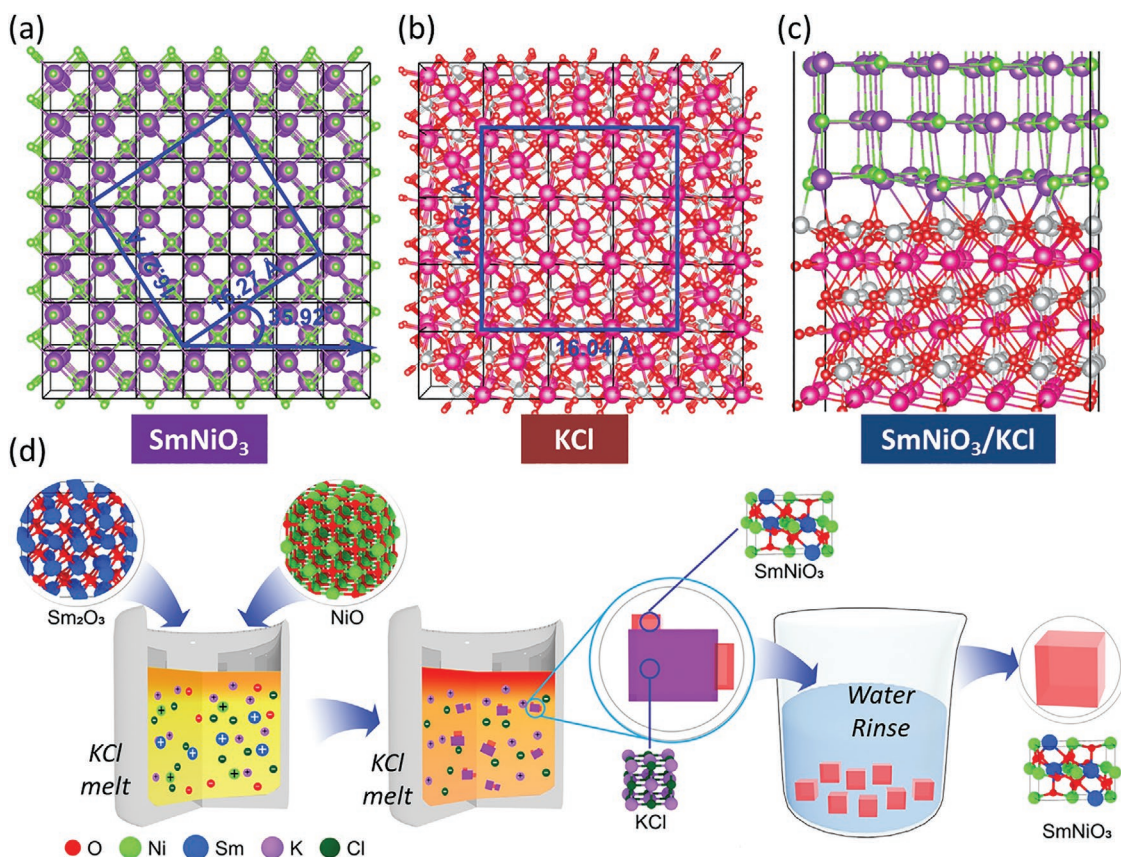


**Figure 1.** Top view of a) KCl (001) surface and b) SmNiO<sub>3</sub> (010) surface and c) side view of SmNiO<sub>3</sub> (010)/KCl (001) interface. The primitive- and supercell of both SmNiO<sub>3</sub> and KCl surfaces are indicated by the black and blue boxes. The purple, green, silver, red and strawberry spheres refer to K, Cl, Ni, O and Sm atoms, respectively. d) Schematic illustrations of as-proposed synthetic approach for *Re*NiO<sub>3</sub> based on the KCl molten-salt assisted heterogeneous nucleation process.

rare-earth composition occupying the A-site of the perovskite structure makes it possible to achieve more continuous adjustment<sup>[7–10]</sup> of the electronic structure and metal to insulator transition behaviors for as-synthesized *Re*NiO<sub>3</sub>. This is demonstrated in Figure 3b, where the  $T_{MIT}$  of SmNiO<sub>3</sub> was effectively reduced to 45 °C via Nd substitution, while Eu substitution of Sm elevated the  $T_{MIT}$  to 115 °C.

The largely simplified batch synthesis of *Re*NiO<sub>3</sub> paves the way to explore the emerging electronic transportations and functionalities, beyond their conventional metastable states, by further imparting high pressures that triggers their unstable electronic structures.<sup>[22–26]</sup> Although the  $T_{MIT}$  of *Re*NiO<sub>3</sub> was previously reported to reduce linearly with the imparted high pressures,<sup>[22–24]</sup> the respective regulations in electronic structures and transportations for the individual insulating and metallic phases is yet unclear. It is worth noting that the temperature associated material functionality beyond MIT indeed exists, as demonstrated by the recently discovered negative TCR thermistor transportation in the insulating phase of *Re*NiO<sub>3</sub> at a broad temperature range far below  $T_{MIT}$ .<sup>[10,11]</sup> Analogically, whether there could be any more emerging material functionalities existing within the individual insulating or metallic phased *Re*NiO<sub>3</sub> associated to high pressures beyond MIT is worthy to be explored.

Following the above considerations, we further investigate the structure and electronic transportation properties of SmNiO<sub>3</sub> under extreme conditions of high pressures up to 10 GPa. As illustrated in the right upper inset of Figure 3a, high pressures were imparted upon SmNiO<sub>3</sub> within a diamond anvil cell (DAC), while the resultant variations in crystal structures were in situ characterized by using XRD and refinement. Figure 6 (Supporting Information) shows the XRD patterns of SmNiO<sub>3</sub> in situ measured under various magnitudes of high pressures and more details about the refinement process. Plotting the lattice volume as a function of pressure as shown in Figure 3a indicates an approximately linear shrinkage in the unit cell of SmNiO<sub>3</sub> induced by high pressures by  $-0.8 \text{ \AA}^3$  per GPa. Nevertheless, the shrinkages are not homogeneously allocated within the three dimensions. This is demonstrated in Figure 3b that shows the pressure dependence of the orthorhombic lattice parameters up to the maximum pressure of 13.7 GPa. It can be seen that increasing the pressure first enhances the difference in *a* and *b* parameters until reaching 5.3 GPa, after which the difference in *a* and *b* becomes smaller. The complexity in the various pressure dependence in *a*, *b*, and *c* indicates a compliant pressure response within the lattice of SmNiO<sub>3</sub> via inhomogeneously distorting or tilting the NiO<sub>6</sub> octahedron, and the resultant impact on the electronic structure and correlated electronic transportations are further expected.

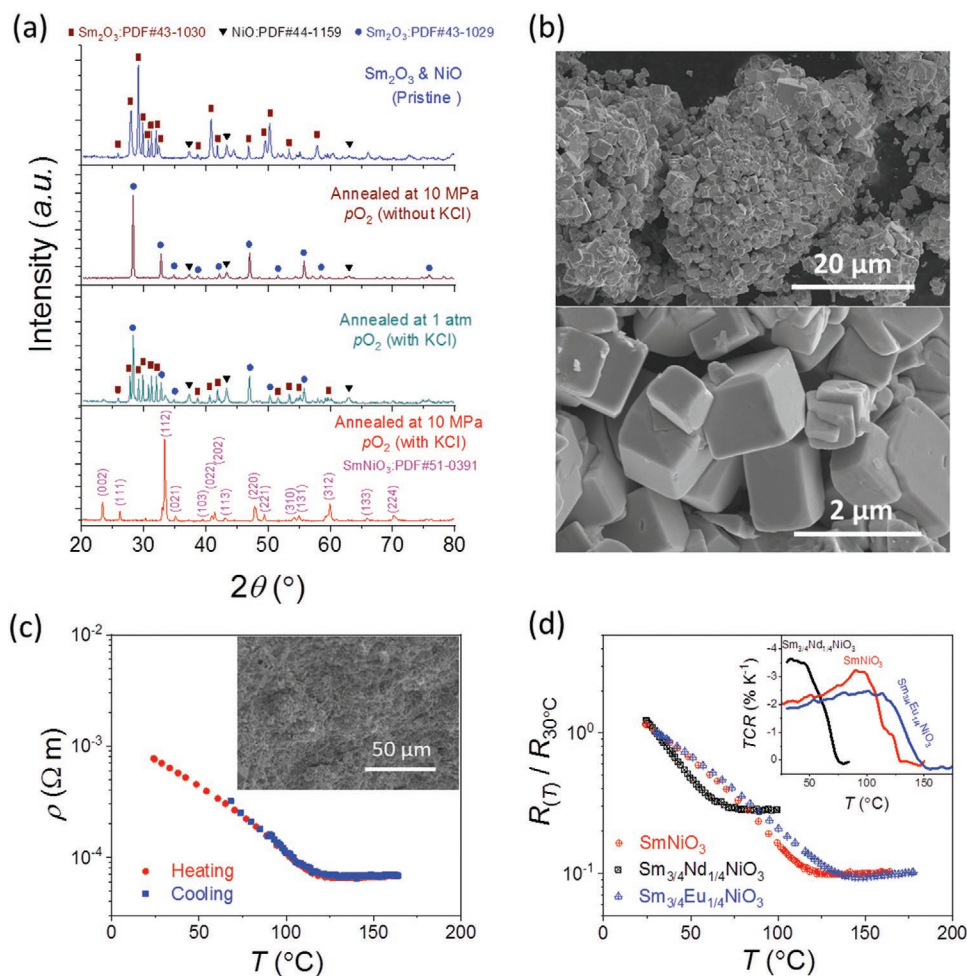


**Figure 2.** a) X-ray diffraction patterns of as-synthesized SmNiO<sub>3</sub> powder, compared to the ones from other typical conditions, such as mixing the pristine oxide precursors, high pressure annealing without KCl and normal pressure annealing with KCl. b) Morphology of as-synthesized SmNiO<sub>3</sub> powder from scanning electron microscopy at various magnifications. c) Temperature dependence of the resistivity for as-synthesized SmNiO<sub>3</sub> polycrystalline bulk sample with the inset showing its cross-sectional morphology from scanning electron microscopy. d) Metal to insulator transition behavior for as-synthesized SmNiO<sub>3</sub>, Nd<sub>0.25</sub>Sm<sub>0.75</sub>NiO<sub>3</sub>, Eu<sub>0.25</sub>Sm<sub>0.75</sub>NiO<sub>3</sub> polycrystalline bulk samples demonstrated by their temperature dependence of the resistivity and temperature coefficient of resistance (TCR, shown in inset).

Figure 3c shows the resistivity ( $\rho$ ) in situ characterized for SmNiO<sub>3</sub> under various magnitudes of externally imparted high pressure ( $P$ ) range up to 22 GPa at room temperature, where a reducing  $\rho$ - $P$  tendency is observed following a  $P^{-0.75}$  relationship. The  $R$ - $T$  tendencies in situ measured for SmNiO<sub>3</sub> under various magnitudes of the imparted high pressures are compared in Figure 3d, while their respective  $\ln[R(T)/R_0]$ - $T^{-1}$  relationships are demonstrated in Figure S7 (Supporting Information). The unpressurized SmNiO<sub>3</sub> exhibits a negative  $R$ - $T$  tendency within the temperature range of 2–300 K, and this is in agreement with the negative TCR thermistor transportation behavior as previously reported for the insulating phase of SmNiO<sub>3</sub>.<sup>[10,11]</sup> Fitting its  $R$ - $T$  tendency by  $R(T) = R_0 \exp[E_a / (k_B T)]$ , where the  $E_a$  is the activation energy and  $k_B$  represents the Boltzmann constant, indicates a thermal activation energy ( $E_a$ ) of  $\approx 0.03$  eV (see the inset of Figure 3d) required for the carrier transportation among the NiO<sub>6</sub> octahedrons via a hopping mode.<sup>[10,28]</sup> In contrast, imparting high pressures of 1.2–5.0 GPa significantly reduces the temperature dependence

of the resistivity, resulting in  $E_a$  approaching to zero by fitting their  $R$ - $T$  tendency within the investigated range of temperature. It is also worth noting that the sharpness in the metal to insulator transitions is reduced by imparting high pressures upon SmNiO<sub>3</sub>, while the respective transition temperature at the high-pressured unstable states ( $T_{US-MIT}$ ) is descended (see a closer comparison of  $R$ - $T$  in Figure S8, Supporting Information).

In Figure 4a, the respective magnitude of  $T_{US-MIT}$  is demonstrated as a function of the magnitude of imparted high pressures ( $P$ ) upon SmNiO<sub>3</sub>. In contrast to the linear reduction of  $T_{US-MIT}$  with  $P$  as reported previously for the less metastable ReNiO<sub>3</sub> such as NdNiO<sub>3</sub> and PrNiO<sub>3</sub>,<sup>[22–24]</sup> as-observed  $T_{US-MIT}$ - $P$  tendency for SmNiO<sub>3</sub> better follows a  $\lg(T_{US-MIT}) = -0.13P + 2.6$  tendency ( $T_{US-MIT}$  with unit in K, while  $P$  in GPa). This is more clearly demonstrated in Figure S9 (Supporting Information), where a better linearity is observed for  $\lg(T_{US-MIT})$ - $P$  compared to the previously expected  $T_{US-MIT}$ - $P$ . Noticing that the presently proposed  $\lg(T_{US-MIT})$ - $P$  linear tendency can indeed also better fit

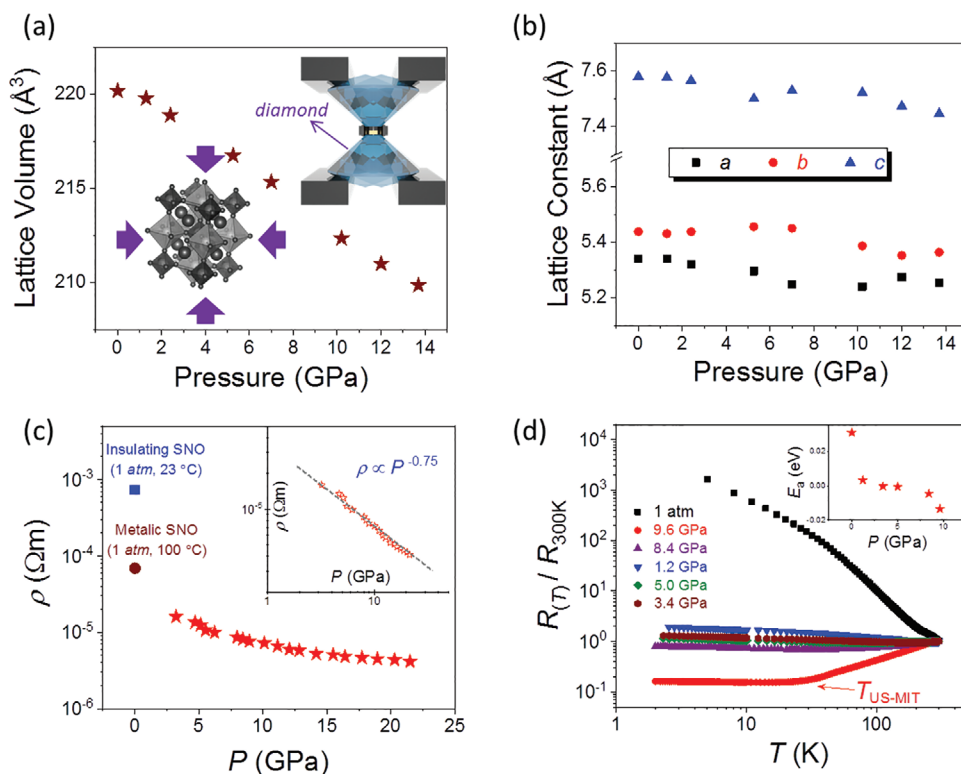


**Figure 3.** a) The volume of  $\text{SmNiO}_3$  unit cell and b) the respective lattice constants plotted as a function of pressure, which are obtained from the refinement of their X-ray diffraction patterns measured in situ under high pressures. The upper right inset in (a) illustrates the construction of the diamond anvil cell (DAC) used in this work to generate high pressures, while the left bottom inset illustrates the crystal structure of  $\text{SmNiO}_3$ . c) Resistivity ( $\rho$ ) of  $\text{SmNiO}_3$  at room temperature measured as a function of the magnitude of as-imparted high pressures. d) The temperature tendency of resistance ( $R-T$ ) measured for  $\text{SmNiO}_3$  under various magnitudes of pressures. The inset shows the activation energy ( $E_a$ ) derived from their  $\ln[R(T)/R_0]-T^{-1}$  relationship for  $\text{SmNiO}_3$  under various pressures.

some previously reported pressure tendencies for  $\text{NdNiO}_3$  and  $\text{PrNiO}_3$  by refs. [22, 24] (Figure S10, Supporting Information).

In Figure 4b, we further compare the kinetic related variations in the  $R-T$  tendencies, e.g., measured first in the cooling down process and afterwards the heating up process, for the unstable metallic phase of  $\text{SmNiO}_3$  under 9.6 and 8.4 GPa. A clear hysteresis is observed in the  $R-T$  tendencies measured in the two different processes across the entire temperature range associated with the unstable metallic phase, which was previously not observed in the conventional metallic  $\text{ReNiO}_3$ .<sup>[8–10]</sup> These observations indicate a phonon excited hysteric and gradual variations in electronic structures of the unstable metallic phase of  $\text{SmNiO}_3$ , while as observed hysteresis loop implies the presence of energy deposition and exchanges.

In contrast to the conventional correlated oxides in their thermodynamically stable states, the high pressure triggered nonequilibrium introduces an additional freedom in manipulating the orbital configurations associated to  $P$  apart from  $T$ . At a high compressive unstable metallic state, the subtle variation in lattice vibrations with changing temperatures is related to extra energy exchanges with the external environment associated to the pressure applied work. This results in the kinetic (or process) dependence in the  $R-T$  tendency at a constant  $P$ , noticing that the electronic orbital configurations within  $\text{ReNiO}_3$  are ultrasensitive to the subtle structural variations via altering the temperature. In Figure S11 (Supporting

Information), we further estimate the difference in Coulomb orbital energy for unstable metallic phase of  $\text{SmNiO}_3$  at the same  $T$  and  $P$  but associated with the respective heating up and cooling down processes. Since the difference in orbital energy states is reflected by the variations in carrier activation energy ( $E_{a,\text{Cool}}$  and  $E_{a,\text{Heat}}$ ), integrating  $(E_{a,\text{Heat}}-E_{a,\text{Cool}})$  over temperature indicates the relative variations in Coulomb orbital energies between the two processes. Following this understanding, there is a postponed energy releasing (up to 0.1 and 0.02 eV under 9.6 and 8.4 GPa, respectively) at the beginning of the afterwards heating up process, compared to the initial cooling down the same  $T$  and  $P$ .

The above demonstrations clearly demonstrate the distinguished electronic transportation characters resultant from the high pressure induced unstable electronic states within both metallic and insulating  $\text{ReNiO}_3$  that are not achievable in conventional metals and semiconductors. In Figure 4c, their temperature dependences in electronic conductance ( $\sigma$ ) are further compared to typical metals, saturating metals, as well as the conventional metallic and insulating  $\text{ReNiO}_3$ . As its electronic structure illustrated in Figure 4d left, the  $E_g$  for conventional insulating phase  $\text{SmNiO}_3$  is expected to be negatively related to the temperature via gradual orbital transitions that results in the negative TCR thermistor transportation behavior.<sup>[10]</sup> Imparting 1 GPa external pressure upon the insulating phase of  $\text{SmNiO}_3$  merges the conduction and valance bands that effectively

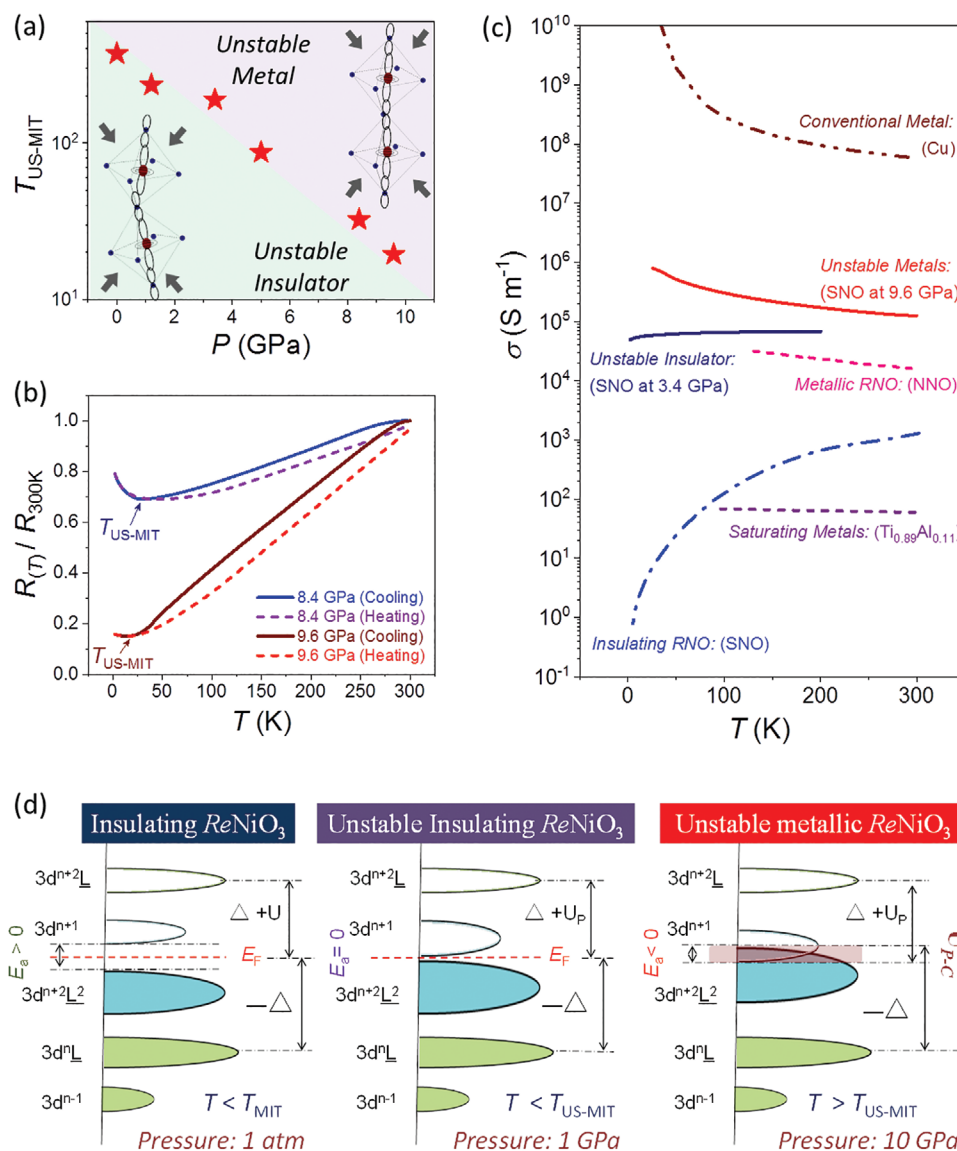


**Figure 4.** a) Metal to insulator transition temperature at a pressure induced unstable state ( $T_{US-MIT}$ ) plotted as a function of the magnitude of the externally imparted high pressure ( $P$ ). b) Hysteresis observed in the  $R$ - $T$  tendency of unstable metallic  $\text{SmNiO}_3$  under 8.4 and 9.6 GPa measured first by cooling down and afterwards heating up. c) Comparing the temperature-dependent electronic conductance ( $\sigma$ ) of the metastable insulating and metallic phase  $\text{SmNiO}_3$  achieved in this work with the ones from typical metals, saturating metals, as well as the conventional phase of metallic and insulating rare-earth nickelates. d) Illustrating the orbital configurations for the conventional insulating phase (left), pressured unstable insulating phase (middle) and further pressured unstable metallic phase (right) of  $\text{SmNiO}_3$ .

reduce its electronic resistivity to the magnitude approaching the metallic phase of  $\text{SmNiO}_3$  even far below  $T_{U-MIT}$ , as illustrated in Figure 4d (middle). It is more interesting to note that even at such a high electronic conductance, the pressured insulating phase of  $\text{SmNiO}_3$  exhibits a nearly constant  $R$ - $T$  tendency similar to saturation metals or bad metals,<sup>[29,30]</sup> as shown in Figure 4c. These observations indicate the formation of a new unstable insulating phase of  $\text{SmNiO}_3$ , the electronic structure of which is more dominated by the imparted pressures ( $U_{\text{Coulomb}}-P$ ). This overwhelms (or freezes) the thermal induced gradual transitions in the electronic structures ( $U_{\text{Coulomb}}-T$ ) of the conventional insulating phase  $\text{SmNiO}_3$  that weakens the temperature dependence in its electronic transportations.

Further elevating the external pressure beyond 10 GPa strengthens more the metallic phase of  $\text{SmNiO}_3$  via overmerging the bandgap (see Figure 4d, right), while the compliance in orbital transitions via pressure regulations is saturated. At such a high pressure range, the orbital configurations and electronic transportations of the unstable metallic phase  $\text{SmNiO}_3$  are demonstrated to be process dependent, as previously indicated by the hysteresis in their  $R$ - $T$  shown in Figure 4b. From a thermodynamic perspective, enhancing the lattice vibrations is expected to promote the tendency that recovers the highly distorted  $\text{NiO}_6$  octahedron toward its equilibrium manner. Following this understanding, elevating temperature will releases the overmerging of conduction and valance bands and increase

the electronic resistivity for the pressured unstable metallic phase  $\text{ReNiO}_3$ . It is also worth noting that its electronic structure of  $\text{ReNiO}_3$  based on  $\text{Ni}^{3+}$  orbital configuration can be further driven toward electron localized multiple states via gradually generating oxygen vacancy.<sup>[31]</sup> This also brings in opportunities to further explore new electronic phases of  $\text{ReNiO}_3$  combining high pressure regulations and electron doping.

### 3. Conclusion

We developed a molten-salt assisted heterogeneous nucleation approach that effectively achieves batch synthesis of metastable rare-earth nickelates with flexibly adjustable rare-earth compositions. In contrast to the conventional synthesis of their powder materials via high pressure solid state reactions, herein the Ni-/Re-containing precursors were dissolved within the liquid phase of KCl molten salt that largely enhances their reaction homogeneity. Owing to the surface coherency and chemical bonding between  $\text{ReNiO}_3$  (010) and KCl (001), reducing the temperature below the melting point of KCl results in heterogeneous coprecipitation of  $\text{ReNiO}_3$  that can be simply separated via water rinsing. The elevated effectiveness in synthesizing metastable  $\text{ReNiO}_3$  further paves the way to explore their correlated transportations under high pressure in the range of 1–10 GPa. High pressure triggers the formation of unstable insulating and metallic electronic states with distinguished transportation behaviors beyond conventional. For example, the unstable insulating  $\text{SmNiO}_3$  (e.g., several GPa) keeps similar small temperature dependence in electronic transportation, compared to saturation or bad metals, at a much higher electronic conductance by two to three orders. Furthermore, hysteresis is clearly observed in the  $R$ - $T$  tendency of unstable metallic  $\text{SmNiO}_3$  (e.g., 10 GPa) measured via cooling down and heating up, revealing its kinetic-related electronic transportation at both freedoms of thermal and compressing regulations.

### Supporting Information

Supporting Information is available from the Wiley Online Library or from the author.

### Acknowledgements

This work was supported by National Natural Science Foundation of China (No. 61674013) and Beijing New-star Plan of Science and Technology (No. Z191100001119071). In addition, this work was also partly supported by the Opening Project of State Key Laboratory of High Performance Ceramics and Superfine Microstructure (Project No. SKL201802SIC.)

### Conflict of Interest

The authors declare no conflict of interest.

### Author Contributions

J.C. proposed the scientific ideas, planned for the present work, performed partially the electronic transportation measurements, analyzed the data; and write the manuscript. Z.L. grew the  $\text{ReNiO}_3$

materials under the supervision of J.C. and N.C. H.D. performed the high pressure XRD and electrical transportation experiments together with Z.F., Z.C., B.C. advised by H.-K.M. V.W. performed the first principle calculations.

### Keywords

correlated semiconductors, high pressures, metastable materials, oxides, perovskites

Received: February 2, 2020

Revised: March 12, 2020

Published online:

- [1] K. Kim, M. W. Schulze, A. Arora, R. M. Lewis III, M. A. Hillmyer, K. D. Dorfman, F. S. Bates, *Science* **2017**, 356, 520.
- [2] Z. Li, K. G. Pradeep, Y. Deng, D. Raabe, C. C. Tasan, *Nature* **2016**, 534, 227.
- [3] C. Chen, J. Avila, H. Arezki, V. L. Nguyen, J. Shen, M. Mucha-Kruczyński, F. Yao, M. Boutchich, Y. Chen, Y. H. Lee, M. C. Asensio, *Nat. Mater.* **2018**, 17, 450.
- [4] A. P. Drozdov, M. I. Erements, I. A. Troyan, V. Ksenofontov, S. I. Shylin, *Nature* **2015**, 525, 73.
- [5] Ho-K Mao, X.-J. Chen, Y. Ding, B. Li, L. Wang, *Rev. Mod. Phys.* **2018**, 90, 015007.
- [6] A. P. Drozdov, P. P. Kong, V. S. Minkov, S. P. Besedin, M. A. Kuzovnikov, S. Mozaffari, L. Balicas, F. F. Balakirev, D. E. Graf, V. B. Prakapenka, E. Greenberg, D. A. Knyazev, M. Tkacz, M. I. Erements, *Nature* **2019**, 569, 528.
- [7] G. Catalan, *Phase Transitions* **2008**, 81, 729.
- [8] M. T. Escote, A. M. L. da Silva, J. R. Matos, R. F. Jardim, *J. Solid State Chem.* **2000**, 151, 298.
- [9] I. V. Nikulina, M. A. Novojilova, A. R. Kaulb, S. N. Mudretsovab, S. V. Kondrashov, *Mater. Res. Bull.* **2004**, 39, 775.
- [10] J. Chen, H. Hu, J. Wang, T. Yajima, B. Ge, X. Ke, H. Dong, Y. Jiang, N. Chen, *Mater. Horiz.* **2019**, 6, 788.
- [11] J. Chen, H. Hu, J. Wang, C. Liu, X. Liu, Z. Li, N. Chen, *ACS Appl. Mater. Interfaces* **2019**, 11, 34128.
- [12] J. Shi, S. D. Ha, Y. Zhou, F. Schoofs, *Nat. Commun.* **2013**, 4, 2676.
- [13] D. Li, K. Lee, B. Y. Wang, M. Osada, S. Crossley, H. R. Lee, Y. Cui, Y. Hikita, H. Y. Hwang, *Nature* **2019**, 572, 624.
- [14] J. Chen, W. Mao, B. Ge, J. Wang, X. Ke, V. Wang, Y. Wang, M. Döbeli, W. Geng, H. Matsuzaki, J. Shi, Y. Jiang, *Nat. Commun.* **2019**, 10, 694.
- [15] Y. Zhou, X. Guan, H. Zhou, K. Ramadoss, S. Adam, H. Liu, S. Lee, J. Shi, M. Tsuchiya, D. D. Fong, S. Ramanathan, *Nature* **2016**, 534, 231.
- [16] F. Zuo, P. Panda, M. Kotiuga, J. Li, M. Kang, C. Mazzoli, H. Zhou, A. Barbour, S. Wilkins, B. Narayanan, M. Cherukara, Z. Zhang, S. K. R. S. Sankaranarayanan, R. Comin, K. M. Rabe, K. Roy, S. Ramanathan, *Nat. Commun.* **2017**, 8, 240.
- [17] Z. Zhang, D. Schwanz, B. Narayanan, M. Kotiuga, J. A. Dura, M. Cherukara, H. Zhou, J. W. Freeland, J. Li, R. Sutarto, F. He, C. Wu, J. Zhu, Y. Sun, K. Ramadoss, S. S. Nonnenmann, N. Yu, R. Comin, K. M. Rabe, S. K. R. S. Sankaranarayanan, S. Ramanathan, *Nature* **2018**, 553, 68.
- [18] H. T. Zhang, F. Zuo, F. Li, H. Chan, Q. Wu, Z. Zhang, B. Narayanan, K. Ramadoss, I. Chakraborty, G. Saha, G. Kamath, K. Roy, H. Zhou, A. A. Chubykin, S. K. R. S. Sankaranarayanan, J. H. Choi, S. Ramanathan, *Nat. Commun.* **2019**, 10, 1651.
- [19] Y. Sun, M. Kotiuga, D. Lim, B. Narayanan, M. Cherukara, Z. Zhang, Y. Dong, R. Kou, C. J. Sun, Q. Lu, I. Waluyo, A. Hunt, H. Tanaka, A. N. Hattori, S. Gamage, Y. Abate, V. G. Pol, H. Zhou,

- S. K. R. S. Sankaranarayanan, B. Yildiz, K. M. Rabe, S. Ramanathan, *Proc. Natl. Acad. Sci. USA* **2018**, *115*, 9672.
- [20] F. Conchon, A. Boule, R. Guinebretière, *Appl. Phys. Lett.* **2007**, *91*, 192110.
- [21] F. Y. Bruno, K. Z. Rushchanskii, S. Valencia, Y. Dumont, C. Carrétéro, E. Jacquet, R. Abrudan, S. Blügel, M. Ležaić, M. Bibes, A. Barthélémy, *Phys. Rev. B* **2013**, *88*, 195108.
- [22] P. C. Canfield, J. D. Thompson, S. W. Cheong, L. W. Rupp, *Phys. Rev. B* **1993**, *47*, 12357.
- [23] X. Obradors, L. M. Paulius, M. B. Maple, J. B. Torrance, A. I. Nazzari, J. Fontcuberta, X. Granados, *Phys. Rev. B* **1993**, *47*, 12353.
- [24] M. Medarde, J. Mesot, P. Lacorre, S. Rosenkranz, P. Fischer, K. Gobrecht, *Phys. Rev. B* **1995**, *52*, 9248.
- [25] J. S. Zhou, J. B. Goodenough, B. Dabrowski, *Phys. Rev. Lett.* **2005**, *94*, 226602.
- [26] J. G. Cheng, J. S. Zhou, J. B. Goodenough, J. A. Alonso, M. J. Martinez-Lope, *Phys. Rev. B* **2010**, *82*, 085107.
- [27] R. Jaramillo, F. Schoofs, S. D. Ha, S. Ramanathan, *J. Mater. Chem. C* **2013**, *1*, 2455.
- [28] E. Ohg, *J. Am. Ceram. Soc.* **2009**, *92*, 967.
- [29] R. Jaramillo, S. D. Ha, D. M. Silevitch, S. Ramanathan, *Nat. Phys.* **2014**, *10*, 304.
- [30] O. Gunnarsson, M. Calandra, J. E. Han, *Rev. Mod. Phys.* **2003**, *75*, 1085.
- [31] M. Kotiuga, Z. Zhang, J. Li, F. Rodolakis, H. Zhou, R. Sutarto, F. He, Q. Wang, Y. Sun, Y. Wang, N. A. Aghamiri, S. B. Hancock, L. P. Rokhinson, D. P. Landau, Y. Abate, J. W. Freeland, R. Comin, S. Ramanathan, K. M. Rabe, *Proc. Natl. Acad. Sci. USA* **2019**, *116*, 21992.